Polymer 293 (2024) 126659

Contents lists available at ScienceDirect

Polymer

journal homepage: www.elsevier.com/locate/polymer

Coexistence of two lamellar populations in poly(ethylene vanillate) reorganized upon heating

Maria Cristina Righetti [a,*], Paola Marchese [b], Dario Cavallo [c], Annamaria Celli [b], Carla Marega [d,**]

[a] CNR-IPCF, National Research Council – Institute for Chemical and Physical Processes, Via Moruzzi 1, 56124, Pisa, Italy
[b] Department of Civil, Chemical, Environmental and Materials Engineering, University of Bologna, Via Terracini 28, 40131, Bologna, Italy
[c] Department of Chemistry and Industrial Chemistry, University of Genova, Via Dodecaneso 3, 16146, Genova, Italy
[d] Department of Chemical Sciences, University of Padova, Via Marzolo 1, 35131, Padova, Italy

ARTICLE INFO

Keywords:
Lamellar populations
Recrystallization
Multiple melting behavior
Wide-angle X-ray scattering
Small-angle X-ray scattering

ABSTRACT

The structural evolution of poly(ethylene vanillate) (PEV) crystals, after isothermal crystallization at $T_c = 180$ °C, was explored by synchrotron wide-angle and small-angle X-ray scattering (WAXS and SAXS) measurements. The WAXS/SAXS analyses proved that an additional more perfect crystal population starts to grow exactly in correspondence of the exotherm displayed by the specific heat capacity curve. The study ascertained that two different reorganization/recrystallization mechanisms occur upon heating: the more perfect crystals originate from a recrystallization process, whereas the original crystals undergo small and progressive perfection maybe without previous complete fusion. Deconvolution of the double Lorentz-corrected SAXS profiles was performed to calculate the temperature evolution of the lamellar thickness for the original and additional crystal populations. The two crystal populations appear to differ substantially in the temperature evolution of the lamellar and amorphous thicknesses. Hypotheses on the relative location of the two different crystal stacks as well as on the possible thermodynamic reason that triggers the formation of the more perfect crystal population have been formulated.

1. Introduction

Nowadays it is urgent to consolidate the transition from an economy based on fossil-derived materials to a biobased and circular materials economy, where building blocks and polymers are sourced from biomass and bio-waste. This transition presents the advantage to exploit the heteroatom-rich natural feedstock to redesign many synthetic polymers. This evolution requires the development of new processes that, starting from bio-feedstocks, make available molecules and monomers by transforming specific bio-derived compounds into building blocks for the appropriate polymerization strategies.

In this context, lignin is often used as feedstock of molecules that can be building blocks to produce semi-aromatic polyesters [1,2]. Lignin is the second most abundant natural polymer on earth after cellulose. It is cheap and largely available in the form of bio-waste. From lignin it is possible to obtain a list of aromatics, including vanillin, which represents one of the very few biobased aromatic building blocks available at an industrial scale [1]. Examples of complete biorefineries that move from lignin to the production of polymers have been developed [1,3]. For these reasons, the development of platforms of biobased aromatic compounds, polymers and copolymers, starting from vanillin and some of its derivatives, such as vanillic acid, is of notable impact.

From vanillic acid, poly(ethylene vanillate) (PEV), the first precursor of the series of poly(alkylene vanillate)s, has been obtained by different pathways [4–8]. PEV is a semicrystalline thermoplastic material, characterized by a notable thermal stability and high values of glass transition and melting temperatures. T_g values that can be found in the literature vary in the range from 61 to 80 °C, mainly depending on the molecular weights, which in general are relatively low [4,8,9]. The melting process of the PEV crystals occurs in a wide temperature range, with the maximum located between 239 and 266 °C [4,9]. These data, which are in agreement with the expected rigid molecular structure of the monomeric unit, due to the presence of the benzene ring in the main chain, are comparable with those of poly(ethylene terephthalate) (PET)

* Corresponding author.
** Corresponding author.
E-mail addresses: cristina.righetti@pi.ipcf.cnr.it (M.C. Righetti), carla.marega@unipd.it (C. Marega).

https://doi.org/10.1016/j.polymer.2023.126659
Received 14 November 2023; Received in revised form 29 December 2023; Accepted 30 December 2023
Available online 30 December 2023

(T_g = 80 °C and T_m = 250 °C) [8].

PEV is a relatively recent polymer: few studies are reported in the literature on its properties. Crystallinity is generally high (around 40–50 %), which induces a notable brittleness in the material [7–10]. To improve ductility and toughness, the addition of soft co-units through copolymerization has been utilized to produce PEV-based materials with lower crystallinity and higher chain mobility [5,7,9]. However, PEV crystallinity decreases with increasing the molecular weight [8]. Crystallization rates higher or lower than that of PET have been measured [8,9]. These conflicting results could be ascribed to different reasons, such the amounts of catalyst used, which could act as nucleating agent, different structure regularity, different molecular weight and percentage of chain ends.

The PEV melting behaviour is multiple both after non-isothermal and isothermal crystallizations [8,9]. The multiple melting behaviour that often is observed in polyesters is generally associated with partial melting, followed by recrystallization and remelting [11], or with the presence of polymorphic forms [12,13] or crystalline populations with different stability and morphology [14–16]. A well-defined exotherm is observed upon heating after crystallization at temperatures lower than 200 °C [8,9]. This exotherm is conversely absent after crystallization at high temperatures [8]. A full comprehension of this behaviour has not yet been reached.

The present study focuses on the PEV multiple melting behaviour after isothermal crystallization below 200 °C. The aim was to investigate in detail the structural changes occurring upon heating and identify the reorganization process that causes the exothermal event. Synchrotron X-ray technique was utilized: wide-angle and small-angle X-ray scattering measurements were performed in parallel with a thermal investigation. The final purpose of the present study is an increasing in-depth knowledge of this new biopolymer, for a better correlation between the chemical structure and its properties and performances.

2. Materials and methods

2.1. Materials

Poly(ethylene vanillate) (PEV) was synthesized and its molecular weight determined as already described [9]. The polymer, with molecular weight (M_n) around 5.000, was used without purification.

2.2. Thermal characterization by differential scanning calorimetry (DSC) and temperature-modulated differential scanning calorimetry (TMDSC)

The calorimetric analysis was carried out by means of a PerkinElmer DSC8000 equipped with an IntraCooler 2 as refrigerating system and calibrated with high purity standards. The measurements were performed under nitrogen flow. To gain accurate heat capacity curves, each heating scan was accompanied by a blank run with an empty pan. The PEV samples (ca. 10 mg) were initially heated at 20 K min^{-1} to 290 °C and kept at high temperature for 2 min, to cancel the previous thermal history. After this thermal treatment, the samples were cooled to 120, 140, 160, 180 and 200 °C at 150 K min^{-1}, and maintained at these crystallization temperatures (T_c) for times sufficient to obtain the leveling of the heat flow rate signal after the exothermal peak (3 min at 120 °C, 4 min at 140 °C, 5 min at 160 °C, 5 min at 180 °C, and 14 min at 200 °C). The melting behavior after complete crystallization was investigated by heating the PEV samples at 10 K min^{-1} directly from the various T_cs, to obtain apparent specific heat capacity ($c_{p,app}$) curves. The PEV sample crystallized at 180 °C for 5 min was also analysed (*i*) at different heating rates (2, 5, 10 and 20 K min^{-1}) and (*ii*) by TMDSC, with a saw-tooth modulation temperature program, at the average heating rate of 2 K min^{-1}, with a temperature amplitude (A_T) of 0.5 K and a modulation period (p) of 60 s, to obtain average specific heat capacity ($c_{p,ave}$) and reversing specific heat capacity ($c_{p,rev}$) curves. From the average components of the modulated temperature and heat flow rate, the $c_{p,ave}$ curve was derived, whereas, from the periodic components, the $c_{p,rev}$ curve was obtained according to Eq. (1) [17,18]:

$$c_{p,rev}(\omega,T) = \frac{A_{HF}(T)}{A_T(T)}\frac{K(\omega)}{m\omega} \quad (1)$$

where A_{HF} and A_T are the amplitudes of the first harmonic of the modulated heat flow rate and temperature, respectively, ω is the fundamental frequency of temperature modulation ($\omega = 2\pi/p$), m is the mass of the sample, and $K(\omega)$ is the frequency-dependent calibration factor, which is 1.07 ± 0.02 for p = 60 s [19].

2.3. Wide-angle and small-angle X-ray scattering (WAXS and SAXS) characterization

Simultaneous WAXS and SAXS measurements were performed in transmission geometry using synchrotron radiation at the beamline BM26 of the European Synchrotron Radiation Facility (ESRF), Grenoble, France. The sample powder was fitted in glass capillary of 2 mm diameter, which was inserted in a LINKAM hotstage for the application of the thermal history. X-ray scans were collected each 2 K during the heating ramp at 10 K min^{-1}. The magnitude of the scattering vector q defined by $q = (4\pi/\lambda)\sin\theta$, where λ = 0.10332 nm (12 keV) is the wavelength of the X-ray source and 2θ the scattering angle, was calibrated using α-Al_2O_3 (WAXD) and silver behenate (SAXS). The sample-to-detector distance were 0.279 m and 2.94 m for WAXS and SAXS, respectively. Patterns were recorded with Pilatus 300 K–W (WAXS) and Pilatus 1 M (SAXS) detectors. The radial integrations of the 2D patterns were performed using home-built routines of BUBBLE software package.

To eliminate the scattering from the glassy sample container, a scan of the empty capillary was performed and subtracted from all the WAXS and SAXS profiles, after correction for the different transmission coefficients of the capillary and the capillary with the sample.

WAXS crystallinity degree was calculated from the ratio between the integrated scattering of the crystalline peaks (A_c) and the total one ($A_c + A_a$) [20]. Air and incoherent scattering were considered using a Chebyshev function with two parameters. The peak profile was simulated by a Pearson VII function and the amorphous profile was calculated starting from the pattern of the totally melted sample and scaling it appropriately on each pattern.

As regards the SAXS measurements, due to the large accessible q range, for each temperature the background contribution from electron density fluctuations in the amorphous phase (I_b), supposed constant in the entire q interval, was assumed equal to SAXS intensity measured at q = 4 nm^{-1}, and subtracted from the relative SAXS profile. The Lorentz-corrected SAXS intensities were achieved after multiplication by q^2. Being the lower limit of the experimental SAXS patterns at about q = 0.2 nm^{-1}, the Iq^2 curves were extrapolated at q = 0 with a second order polynomial between q = 0.2 nm^{-1} and q = 0 [21,22].

3. Results and discussion

3.1. Melting behavior of PEV as a function of T_c

Fig. 1 displays the $c_{p,app}$ curves after isothermal crystallization at 120 ≤ T_c ≤ 200 °C upon heating at 10 K min^{-1} from the respective T_cs. All the curves display a similar melting behavior, substantially independent of T_c, in perfect agreement with a previous study [8]. A first small peak can be barely detected at temperatures slightly above T_c. This peak is frequently observed in semi-crystalline polymers. It has been generally associated to the fusion of less perfect secondary crystals [23] and also rationalized as the balance of initial melting and the successive recrystallization that occurs at sufficiently low heating rates [11]. Sometimes the first peak, also called "annealing peak" has been connected to the devitrification of the rigid amorphous fraction (RAF) formed during isothermal crystallization [24,25]. As information on the temperature

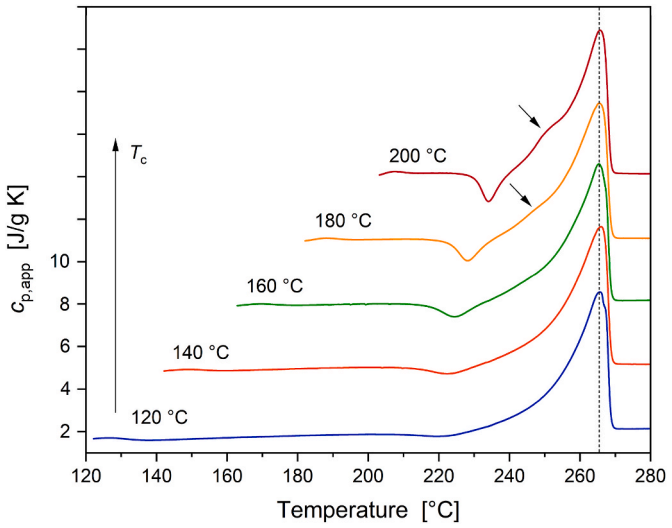

Fig. 1. Apparent specific heat capacity ($c_{p,app}$) curves of PEV measured at 10 K min^{-1} after isothermal crystallization at the specified T_cs. The ordinate values refer only to the bottom curve. All the other curves are shifted vertically for the sake of clarity. The arrows indicate the shoulder on the low temperature side of the final melting peak after crystallization at the higher T_cs (see discussion in the text).

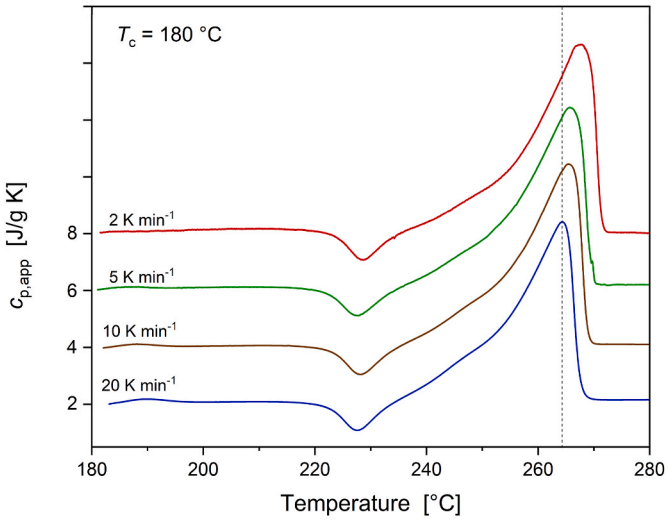

Fig. 2. Apparent specific heat capacity ($c_{p,app}$) curves of PEV measured at the indicated heating rates after isothermal crystallization at T_c = 180 °C. The ordinate values refer only to the bottom curve. All the other curves are shifted vertically for the sake of clarity.

dependence of the RAF in PEV is currently not available, this possible interpretation cannot be verified. At higher temperatures, an exothermic process is well evident in the temperature range 210–240 °C. With increasing T_c, it appears progressively narrower and centered at increasing temperatures. The exotherm precedes a final endotherm, with peak positioned at 266° independently of T_c. The only difference in the final melting peak among the various $c_{p,app}$ curves is a shoulder on the low temperature side, which appears slightly more intense with increasing T_c. It has been demonstrated for several polymers that fusion begins some degrees above T_c [26,27], which means that the PEV melting peak centered at 266 °C undoubtedly originates from significant reorganization/recrystallization processes occurring upon heating, as also attested by the exothermic event. Conversely, the shoulder on the low temperature side of the melting peak could identify the fusion of original, slightly reorganized crystals. With increasing T_c, the original crystals become more and more stable, *i.e.* less prone to reorganizing/-recrystallizing. This leads to the appearance and/or rise of a peak (the shoulder, in the present case) located at lower temperatures with respect to the final melting, with size increasing with T_c [13,28]. The shoulder becomes indeed progressively more evident with increasing T_c, notwithstanding the exothermic process is present in all the $c_{p,app}$ curves plotted in Fig. 1. This confirms that the shoulder is not connected to the fusion of crystals grown during the exothermal event, but to the fusion of original slightly reorganized crystals grown at T_c.

The $c_{p,app}$ curves at different heating rates after crystallization at T_c = 180 °C (see Fig. 2) display an identical melting behavior, with the exotherm located in the same temperature range, which suggests that this exothermic event is not totally kinetically driven, and that thermodynamic bases also play some role. In addition, the final melting peak shifts to higher temperatures with decreasing the heating rate, in agreement with the more important reorganization/recrystallization that can occur at lower heating rates. The peculiarity that the location and area of the exotherm do not to change, whereas in parallel the melting peak moves to higher temperatures by reducing the heating rate means that two different reorganization/recrystallization processes take place during the heating from T_c = 180 °C up to complete fusion.

The analysis of the melting behavior by TMDSC after crystallization at T_c = 180 °C is shown in Fig. 3. The reversing heat capacity ($c_{p,rev}$) derives from the amplitude of the events that follow the temperature

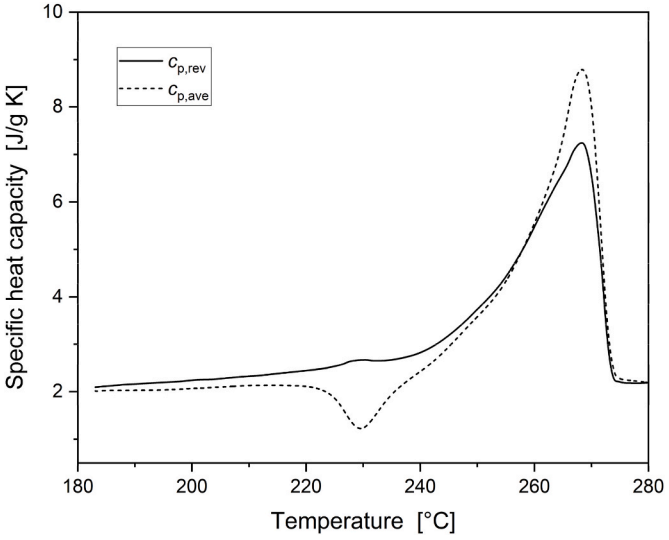

Fig. 3. Reversing specific heat capacity ($c_{p,rev}$) and average specific heat capacity ($c_{p,ave}$) curves of PEV after isothermal crystallization at T_c = 180 °C (p = 60 s, A_T = 0.5 K, average heating rate = 2 K min^{-1}).

modulation (*i.e.* endothermic process in one semi-period and exothermic process in the other semi-period), whereas in $c_{p,ave}$ the released or absorbed heats algebraically sum up [25], so that $c_{p,ave}$ corresponds to $c_{p,app}$ at 2 K min^{-1} (see also Fig. 2). Fig. 3 shows that $c_{p,rev}$ remains higher than $c_{p,ave}$ up to about 260 °C. This means that exothermic processes (additional crystallization and/or reorganization/recrystallization) occur upon heating starting from T_c up to about 260 °C. In correspondence with the exotherm centered at 230 °C in the $c_{p,ave}$ curve, $c_{p,rev}$ exhibits a small peak, which attests that this process partially proceeds reversibly.

To investigate the structural changes induced by heating in a PEV sample crystallized at T_c = 180 °C, combined WAXS/SAXS analysis was performed.

3.2. WAXS analysis of PEV crystallized at T_c = 180 °C as a function of temperature

The temperature resolved WAXS profiles collected upon heating at 10 K min^{-1} after crystallization at T_c = 180 °C are shown in Fig. 4. The WAXS patterns display the main diffraction reflections at q = 9.6, 10.4, 15.0, 15.5, 16.9 and 18.8 nm^{-1}, which, according to the Bragg law, correspond to interplanar distances of 0.65, 0.60, 0.42 0.40, 0.37 and 0.33 nm, respectively. Appearance of additional reflections upon heating is not detected, which excludes crystal structure modification. The increase in temperature does not produce shifts in the position (at most −0.1 nm^{-1}) but only variation of the intensity and width of the WAXS peaks.

Table 1 lists the crystal fraction (X_C^{WAXS}) and the full width of half-maximum (FWHM) of the main WAXS peaks at selected temperatures. The crystal fraction shows an initial decrease, linked to the fusion that occurs in correspondence of the first small peak slightly above T_c. Then it remains constant at 0.39 between 204 and 224 °C. This means that the crystals that melt in this temperature range completely recrystallize/reorganize. Successively, additional melting occurs, because X_C^{WAXS} decreases to 0.35 at about 228 °C. At higher temperatures, X_C^{WAXS} increases again, up to about 245 °C, which is in agreement with the exotherm present in the $c_{p,app}$ (and $c_{p,ave}$) curves. As the fusion between 224 and 228 °C is not visible in the $c_{p,app}$ curves, which conversely display an exothermal signal, it can be supposed that the recrystallization occurring in this temperature range concerns the formation of crystals more stable with respect to the newly melted crystals. These more perfect crystals could be characterized by a lower enthalpy content, which can interpret the $c_{p,app}$ curves resulting from the algebraic sum of the endothermic and exothermic heats.

Analysis of the WAXS profiles points out that between approximately 204 and 220 °C the amplitude at half width of some peaks increases (see Table 1), certainly due to crystallite size reduction as a consequence of the initial crystallinity decrease. Between 228 and 245 °C, the amorphous halo remains the same, but the intensity of the peaks increases and the amplitude at half width decreases (see Table 1), which further confirms refinement of the crystallites. At temperatures higher than 245 °C, X_C^{WAXS} drops, as a consequence of the increase in the amorphous halo, whereas FWHM continues to decrease, until the final melting at 280 °C. Also this further and progressive crystal improvement can be linked to the formation of more perfect crystals.

To further investigate the structural and crystal morphology changes or reorganization phenomena occurring upon heating, a quantitative thorough analysis of the SAXS profiles was performed.

Table 1
Crystal fraction from WAXS profiles (X_C^{WAXS}) and full width of half-maximum (FWHM) of the main WAXS peaks (at q = 9.6, 10.4, 15.0, 15.5, 16.9 and 18.8 nm^{-1}, respectively) calculated at selected temperatures.

T [°C]	X_C^{WAXS}	FWHM					
		q = 9.6 nm^{-1}	q = 10.4 nm^{-1}	q = 15.0 nm^{-1}	q = 15.5 nm^{-1}	q = 16.9 nm^{-1}	q = 18.8 nm^{-1}
180.0	0.48	0.24	0.44	0.47	0.60	0.83	0.96
196.0	0.43	0.24	0.45	0.38	0.60	0.68	0.98
204.0	0.39	0.24	0.45	0.41	0.60	0.70	1.15
215.9	0.39	0.22	0.47	0.41	0.60	0.75	1.15
219.7	0.39	0.22	0.47	0.41	0.60	0.72	1.15
223.7	0.39	0.23	0.47	0.41	0.59	0.72	1.08
227.8	0.35	0.23	0.46	0.41	0.55	0.72	1.00
231.8	0.36	0.23	0.46	0.40	0.53	0.72	1.00
235.6	0.36	0.22	0.44	0.37	0.48	0.72	0.99
241.7	0.37	0.22	0.42	0.37	0.43	0.67	0.96
245.7	0.37	0.20	0.42	0.33	0.43	0.63	0.96
249.7	0.35	0.18	0.40	0.33	0.38	0.61	0.95
253.7	0.34	0.17	0.39	0.31	0.38	0.62	0.89
257.6	0.33	0.17	0.38	0.29	0.38	0.56	0.90
261.6	0.30	0.16	0.37	0.29	0.30	0.58	0.89
265.6	0.25	0.17	0.36	0.32	0.32	0.52	0.90

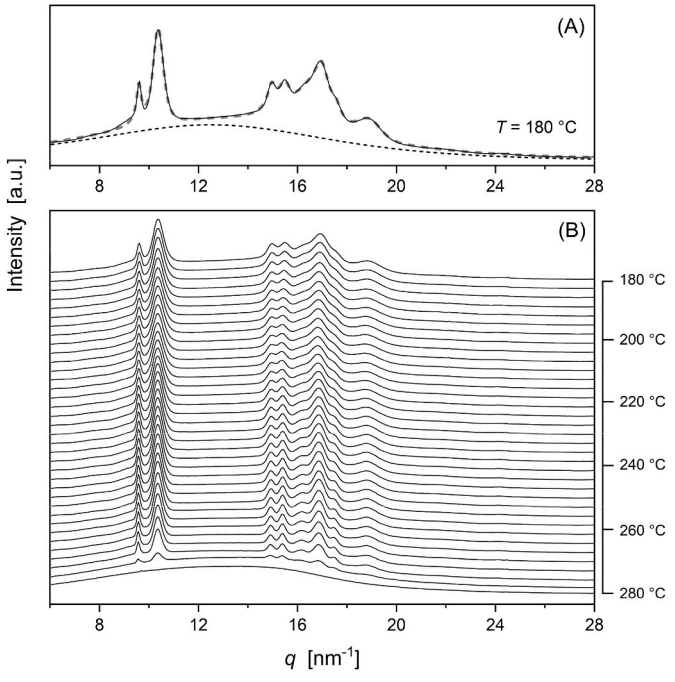

Fig. 4. (A) WAXS pattern of PEV at 180 °C after isothermal crystallization at T_c = 180 °C. The thin black curve is the experimental profile, the thick dashed grey curve is the calculated intensity after peak simulation. The scattering of the amorphous fraction (black short dashed line) is also shown. (B) Temperature-resolved WAXS profiles of PEV upon heating (heating rate: 10 K min^{-1}) after isothermal crystallization at T_c = 180 °C.

3.3. SAXS analysis of PEV crystallized at T_c = 180 °C as a function of temperature

Temperature-resolved Lorentz-corrected SAXS profiles attained upon heating at 10 K min^{-1} after crystallization at T_c = 180 °C are shown in Fig. 5. By increasing the temperature from 180 to about 225 °C, the patterns exhibit a single peak, whose maximum shifts progressively from q = 0.85 to about 0.80 nm^{-1}. Starting from about

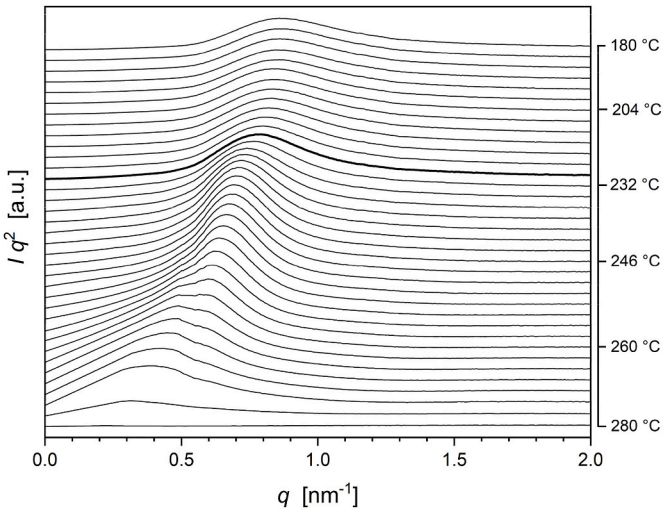

Fig. 5. Temperature-resolved Lorentz-corrected SAXS profiles of PEV upon heating (heating rate: 10 K min^{-1}) after isothermal crystallization at T_c = 180 °C. The thick line marks the appearance of an additional peak in the Iq^2 curves.

227 °C, an additional peak appears at lower q values, firstly as a shoulder, and then as resolved peak. Both these two peaks progressively move to lower q values with increasing the temperature. The intensity of the peaks increases up to approximately 255 °C, and then gradually decreases. Importantly, the temperature at which the additional SAXS peak appears corresponds to the exotherm in the $c_{p,app}$ curves, which leads to connect the exothermic event with the growth of a different and more perfect crystal population.

The occurring of two separate SAXS peaks has been observed for some polymers and connected to the presence of two different crystal organizations [29–33]. For polyethylene, the additional SAXS peak was interpreted as due to lamellar doubling [29,30], generated by sliding motions in the solid state. Conversely, for poly[(R)-3-hydroxybutyrate)], the discontinuous increase in lamellar thickness was ascribed to partial melting and recrystallization [31]. A recent study has proven that also in poly(butylene succinate) lamellae with higher thickness grow upon heating, with the result that two different crystal populations coexist at high temperature [16]. A similar assumption can be applied also to PEV to rationalize the double-peaked SAXS behavior. A more perfect crystal population could grow in addition to the original one upon heating, due to reorganization/recrystallization processes.

To separate the contribution of the two different peaks to the Lorentz-corrected SAXS profiles, a multiple peakfit procedure was applied. An exponentially modified Gaussian function was utilized for the non-linear curve fitting (commercial software OriginPro, OriginLab Corporation):

$$f(q) = y_o + \frac{A}{\tau}\exp\left[\frac{1}{2}\left(\frac{w}{\tau}\right)^2 - \frac{q-q_c}{\tau}\right]\int_{-\infty}^{z}\frac{1}{\sqrt{2\pi}}\exp\left(-\frac{y^2}{2}\right)dy \quad (2)$$

with $z = [(q\text{-}q_c)/w - w/\tau]$, where A is the peak area, τ the peak distortion, w the peak width and q_c the position of the peak maximum. The fitting parameters deduced from the mathematical description of the single slightly asymmetric SAXS profiles at temperatures lower than 225 °C were utilized as initial values for the multiple peak fitting. Some examples of the deconvolution obtained are shown in Fig. 6. Peak fitting was performed only on the Iq^2 curves between 245 and 266 °C: it was impossible to separate the two peaks for lower and higher temperatures.

From the deconvoluted Iq^2 curves, the scattering invariants for the original and the additional more perfect crystal populations (Q_{orig} and Q_{perf}) were calculated according to the definition:

$$Q = \int_0^{\infty} Iq^2 dq \quad (3)$$

The scattering invariant Q is also described as [34–36]:

$$Q = K\alpha_S X_{C,l}(1 - X_{C,l})(\rho_c - \rho_a)^2 \quad (4)$$

where K is a constant, α_S is the volume fraction of the crystal stacks in the sample total volume, $X_{C,l}$ is the linear crystallinity within the stack and ρ_c and ρ_a are the densities of the crystalline and amorphous fractions. The product $\alpha_S X_{C,l}$ corresponds to the volumetric bulk crystallinity X_C.

Fig. 7 displays the temperature dependence of the scattering invariants Q_{orig} and Q_{perf} in the temperature range in which peak fitting was performed. The invariant Q_{orig} relative to the original Iq^2 peak, initially centered at about $q = 0.85$ nm^{-1}, decreases significantly between 245 and 260 °C and more slowly at higher temperatures. The Q_{orig} decrease in the temperature range 245–260 °C can be put into relation with the shoulder observed in the $c_{p,app}$ curves in the same temperature range, which has been associated with the fusion of original, slightly reorganized crystals. Simultaneously with the Q_{orig} decrease, Q_{perf} is found to increase, confirming that the new crystal population, which however starts to develop at lower temperatures (see Fig. 5), originates from the disappearance of the original one and undergoes fusion at higher temperatures. The increase in crystallinity estimated in the temperature range 228–242 °C (see Table 1) also leads to suppose that the growth of the more perfect crystal population occurs via recrystallization of the melted original crystals. Above 260 °C, Q_{perf} decreases. This peculiarity can also be correlated with the melting behaviour shown in Fig. 3, in which from the comparison between $c_{p,rev}$ and $c_{p,ave}$ curves it was deduced that exothermal processes take place upon heating up to about 260 °C. At temperatures higher than 260 °C, the growth of the additional crystal population stops, and both original and more perfect crystals undergo final melting.

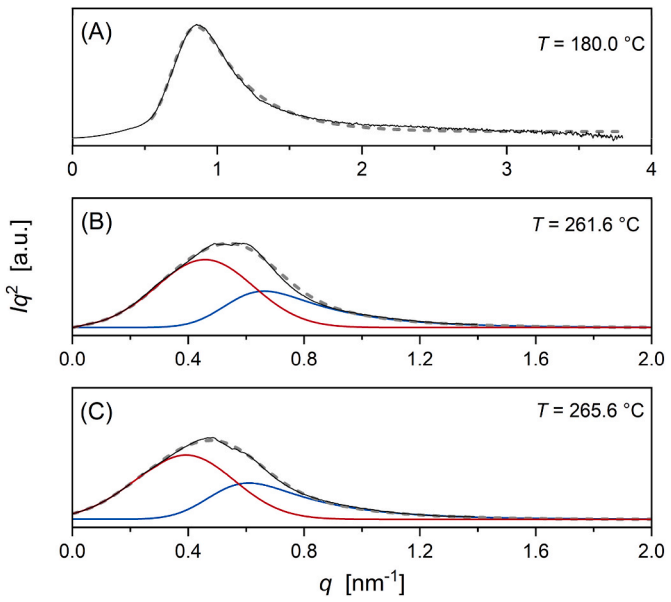

Fig. 6. (A) Example of the peakfit analysis of the Iq^2 profile at $T = 180.0$ °C, which displays a single peak. The fit was obtained by using an exponentially modified Gaussian function. The dashed grey curve is the calculated Iq^2 curve from peak fitting. (B), and (C) Multiple peakfit analysis of the Iq^2 profiles at $T =$ 261.6 and 265.6 °C, which display two partially overlapping peaks. The fit was obtained by using an exponentially modified Gaussian function. The thin black curve is the experimental profile, the blue and red curves are the calculated Iq^2 profiles from peak fitting and the thick dashed grey curve is the sum of the two deconvoluted Iq^2 profiles. (For interpretation of the references to colour in this figure legend, the reader is referred to the Web version of this article.)

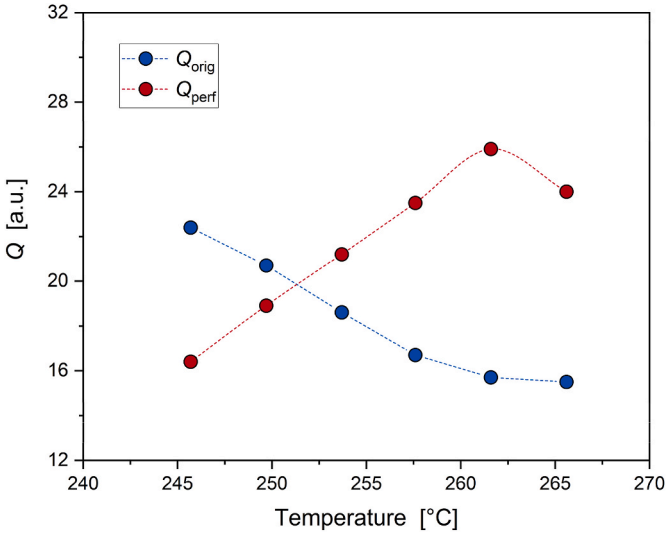

Fig. 7. Temperature evolution of the invariants Q_{orig} and Q_{perf} calculated from the deconvoluted Lorentz-corrected SAXS profiles. The dashed lines are a guide to the eye.

To study and quantify the evolution of the PEV crystal nanostructure upon heating, correlation functions at different temperatures were calculated from the single and deconvoluted Iq^2 curves. The one-dimensional correlation functions $K(z)$, with z corresponding to the direction normal to the stack layers, is defined as [22,37,38]:

$$K(z) = \int_0^\infty Iq^2 \cos(qz)dq \quad (5)$$

From the plot of $K(z)$ as a function of z, the long period of crystalline lamellae stacks can be derived from the position of the first maximum (L_{LB}), whereas the average crystal lamellar or amorphous thickness can be obtained from the linear tangent (l_{tan}) to the initial $K(z)$ decay [35–38]. The correlation functions were calculated from the peak fitted Iq^2 curves, non-deconvoluted in the temperature range 180–241 °C and deconvoluted in the temperature range 245–265 °C.

Fig. 8 shows a comparison between the correlation functions $K(z)$ calculated from the original Lorentz-corrected SAXS profile at 180.0 °C and the corresponding peak fitted curve. The very good matching between the two $K(z)$ curves guarantees the accuracy of the structural parameters that can be derived from the peak fitted curves.

Fig. 8 also displays the correlation functions calculated from the two deconvoluted Iq^2 curves at 261.6 °C, together with the correlation function calculated from the experimental non-deconvoluted SAXS profile. The $K(z)$ curve derived from the sum of the deconvoluted Iq^2 curves is also shown, to be compared with the $K(z)$ curve derived from the experimental Lorentz-corrected SAXS profile. The strong similarity between these two latter $K(z)$ curves confirms that the procedure of peak fitting is able to describe and interpret correctly a complex SAXS profile. From Fig. 8 it can be noted that the first minimum and maximum of the $K(z)$ curve from the experimental Lorentz-corrected SAXS profile are intermediate between those of the $K(z)$ curves derived from the deconvoluted Iq^2 curves.

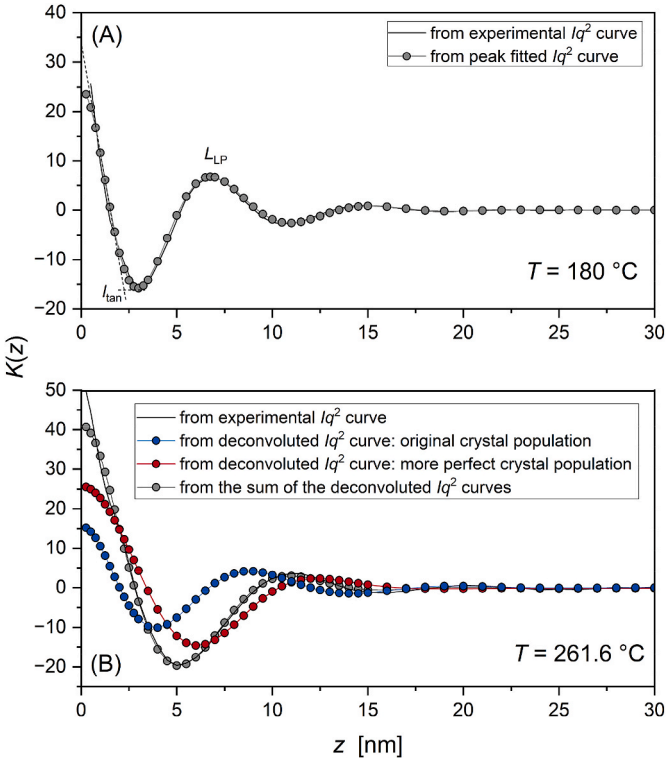

Fig. 8. (A) Comparison between the correlation functions $K(z)$ calculated from the experimental and the peak fitted Lorentz-corrected SAXS profile at T = 180.0 °C. (B) Correlation functions $K(z)$ calculated from the experimental Lorentz-corrected SAXS profile at T = 261.6 °C and from the two deconvoluted Lorentz-corrected SAXS profiles. The $K(z)$ curve derived from the sum of the deconvoluted Iq^2 curves is also shown. The thin black dashed lines in (A) show how the long period L_{LP} and the thickness l_{tan} were estimated.

Table 2 lists the L_{LP} and l_{tan} values derived from the correlation functions of the non-deconvoluted Iq^2 curves up to 227 °C, *i.e.* in the temperature range in which the SAXS profiles display a single peak. By assuming that l_{tan} corresponds to the lamellar thickness (l_c), the linear crystallinity was derived as $X_{C,l,tan} = l_{tan}/L_{LP}$. The $X_{C,l,tan}$ values, collected in Table 2, turn out to be lower than the corresponding crystals fractions calculated by WAXS (see Table 1). This matter appears inconsistent, because $X_{C,l}$ and X_C^{WAXS} are approximately connected by the relationship $X_C^{WAXS} = \alpha_S X_{C,l}$, with α_S, the volume fraction of the lamellar stacks within the total sample, necessarily lower than 1. Table 2 shows that, by assuming $l_{tan} = l_c$, $\alpha_{S,tan}$ is higher than 1. This means that l_{tan} does not corresponds to the lamellar thickness, but to the thickness of the amorphous layer (l_a), and that l_c must be obtained as (L_{LP} - l_a). The last four columns of Table 2 list the correct l_c, l_a, $X_{C,l}$ and α_S values for the original crystal population from 180 to about 230 °C.

The same procedure was applied to the deconvoluted Iq^2 curves for the calculation of L_{LP}, l_c and l_a at temperatures higher than 245 °C, for both the original and the additional more perfect crystal populations. All the dimensional parameters of the crystalline stacks of the original and the more perfect crystal populations are plotted in Fig. 9. The L_{LP}, l_c and l_a values derived from the non-deconvoluted Iq^2 profiles in the temperature range in which the additional crystal population starts to develop (230–242 °C) are also reported. These values are obviously halfway between those pertinent to the two different populations. The linear crystallinity of the original crystal population remains approximately 0.66 also at temperatures higher than 245 °C, whereas $X_{C,l}$ for the more perfect population is slightly lower (around 0.60), due to the lower l_c/l_a ratio.

The lamellar thickness of the original crystals is 4.5 nm at 180 °C, 5.2 nm at 245 °C and 5.8 nm at 260 °C. The lamellar thickness of the more perfect crystals is 5.8 nm at 245 °C, and 7.6 nm at 260 °C. Fig. 9 seems to suggest no significant discontinuity between the lamellar thickness of the original and more perfect crystals at the temperature at which the new crystals start to grow. But with increasing the temperature, the difference in l_c and also l_a markedly increases. In practice, the two crystal populations differ in the temperature evolution of the lamellar and amorphous layer thicknesses. In a previous study on PEV, a change in the spherulite morphology of isothermally crystallized PEV was identified exactly at 235 °C, and associated to the transition from crystallization regime I to regime II, according to the Lauritzen-Hoffman secondary nucleation theory [8]. On the basis of this information, it can be supposed that the more perfect crystals originate truly from a recrystallization process, whereas maybe the original crystals undergo small and progressive perfection without previous complete fusion. In any case, the position of the two different crystal stacks could be

Table 2
Temperature dependence of the long period (L_{LP}), layer thickness from linear tangent to the initial $K(z)$ decay (l_{tan}), linear crystallinity calculated under the assumption $l_{tan} = l_c$ ($X_{C,l,tan}$), volume fraction of the lamellar stacks within the sample calculated under the assumption $l_{tan} = l_c$ ($\alpha_{S,tan}$), amorphous layer thickness (l_a), crystal lamellar thickness (l_c), linear crystallinity ($X_{C,l}$), and volume fraction of the lamellar stacks within the sample (α_S) for the PEV original crystal population in the temperature range 180–230 °C.

T [°C]	L_{LP} [nm]	l_{tan} [nm]	$X_{C,l,tan}$	$\alpha_{S,tan}$	l_a [nm]	l_c [nm]	$X_{C,l}$	α_S
180.0	6.7_5	2.2_5	0.33	1.4	2.2_5	4.5_0	0.67	0.72
196.0	6.9_0	2.3_0	0.33	1.3	2.3_0	4.6_0	0.67	0.65
204.0	7.0_0	2.3_5	0.34	1.2	2.3_5	4.6_5	0.66	0.59
215.9	7.1_5	2.4_0	0.34	1.2	2.4_0	4.7_5	0.66	0.59
219.7	7.2_5	2.4_5	0.34	1.2	2.4_5	4.8_0	0.66	0.59
223.7	7.3_5	2.5_0	0.34	1.1	2.5_0	4.8_5	0.66	0.59
227.8	7.5_0	2.5_5	0.34	1.0	2.5_5	4.9_5	0.66	0.54

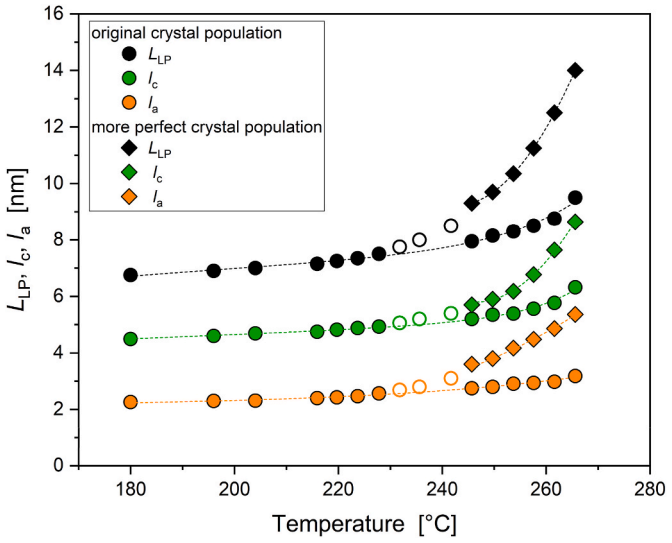

Fig. 9. Temperature dependence of the long period (L_{LP}), lamellar thickness (l_c), and amorphous layer thickness (l_a) of the original and the more perfect crystal populations, calculated from the correlation functions $K(z)$. The open symbols refer to L_{LP}, l_c and l_a values derived from the correlation functions of non-deconvoluted Iq^2 profiles in the temperature range in which the additional crystal population starts to develop. The dashed lines are a guide to the eye.

different: the more perfect crystals could be located in the external regions of the spherulites, which can allow more significant modifications in all the structural parameters upon heating. Conversely, the original crystals could be positioned in more internal areas of the spherulites, where concerted rearrangements are more hindered.

On the basis of the thermodynamic information available at the moment for this new polymer, it is really challenging to identify the reason or the event that triggers the formation of the more perfect crystal population. However, a hypothesis can be expressed. It is known that crystallization at low temperature generally induces simultaneous formation of rigid amorphous fraction (RAF) [39]. At low T_cs, the reduced chain mobility hinders regular chain folding and portions of amorphous segments remain anchored at the basal planes of the lamellae. Conversely, at higher T_cs, RAF vitrification occurs only during the final stages of crystallization or, at sufficiently higher T_cs, it does not occur at all [39]. It was also demonstrated that there exists a temperature limit for the formation and complete mobilization of the RAF [39–42]. For some polymers containing an aromatic ring in the chemical structure, as poly(ethylene terephthalate), poly(butylene terephthalate) and isotactic polystyrene, the RAF temperature limit is close or higher than 200 °C [40,42], whereas this value is lower for aliphatic polyesters, like poly(lactic acid) and poly(3-hydroxybutyrate) (130 and 70 °C, respectively) [39,41]. The chemical structure of PEV may suggest a high RAF temperature limit, close or above 200 °C. This means that crystallization performed at lower temperatures involves RAF formation. The exotherm centered at about 230 °C could be linked to a recrystallization process subsequent to complete devitrification of the RAF developed during crystallization at lower T_cs. Complete mobility of amorphous chains originated from the newly melted crystals can favor the rearrangements necessary to form more perfect structures with higher thermal stability, *i.e.* lamellae with higher thickness and larger lateral dimensions. The hypothesis that the RAF temperature limit is close to 200 °C for PEV will be verified in a forthcoming study.

4. Conclusions

Temperature-dependent synchrotron WAXS/SAXS measurements were used to elucidate the behavior at 10 K min^{-1} of PEV isothermally crystallized at T_c = 180 °C.

The reorganization/recrystallization processes observed by thermal analysis were confirmed by WAXS/SAXS measurements. In particular, the study of the WAXS profiles allowed (*i*) to exclude crystal modification with increasing temperature, (*ii*) to identify an initial decrease in the degree of crystallinity, which corresponds to the small endothermic peak in the $c_{p,app}$ curve just above T_c and (*iii*) to detect a successive increase in the crystalline fraction between 228 and 245 °C, in parallel which a decrease in FWHM, which attests refinement of the crystallites exactly in correspondence of the exotherm displayed by the $c_{p,app}$ curve.

The Lorentz-corrected SAXS profiles shows a single peak, corresponding to an original lamellar population, up to about 225 °C. At higher temperatures, exactly in correspondence of the exotherm in the $c_{p,app}$ curve, an additional peak appears at lower q values, which can be related to the growth of an additional more perfect crystal population. Both these two Iq^2 peaks progressively move to lower q values with increasing the temperature. Their intensity increases up to approximately 255 °C, and then gradually decreases. Deconvolution of the double Lorentz-corrected SAXS profiles was performed to calculate the temperature evolution of the lamellar thickness for the original and the additional crystal populations. The elaboration through the correlation functions proved that the more perfect crystals originate from a recrystallization process, whereas the original crystals undergo small and progressive perfection maybe without previous complete fusion. The two crystal populations appear to differ substantially in the temperature evolution of the lamellar and amorphous thicknesses.

Hypotheses on the relative location of the two different crystal stacks as well as on the possible thermodynamic reason that triggers the formation of the more perfect crystal population have been formulated.

CRediT authorship contribution statement

Maria Cristina Righetti: Conceptualization, Data curation, Formal analysis, Investigation, Methodology, Supervision, Writing – original draft, Writing – review & editing. **Paola Marchese:** Investigation. **Dario Cavallo:** Investigation, Resources, Writing – review & editing. **Annamaria Celli:** Resources, Writing – review & editing. **Carla Marega:** Data curation, Formal analysis, Investigation, Methodology, Writing – original draft, Writing – review & editing.

Declaration of competing interest

The authors declare that they have no known competing financial interests or personal relationships that could have appeared to influence the work reported in this paper.

Data availability

Data will be made available on request.

Acknowledgements

The diffraction experiments (SC5479) were performed on beamline BM26 at the European Synchrotron Radiation Facility (ESRF), Grenoble, France. The authors are grateful to Dr. Martin Rosenthal at the ESRF for the support to the experiments.

References

[1] S. Laurichesse, L. Averous, Chemical modification of lignins: towards biobased polymers, Prog. Polym. Sci. 39 (2014) 1266–1290, https://doi.org/10.1016/j.progpolymsci.2013.11.004.
[2] M. Alherech, S. Omolabake, C.M. Holland, G.E. Klinger, E.L. Hegg, S.S. Stahl, From lignin to valuable aromatic chemicals: lignin depolymerization and monomer separation via centrifugal partition chromatography, ACS Cent. Sci. 7 (2021) 1831–1837, https://doi.org/10.1021/acscentsci.1c00729.
[3] Y. Higuchi, H. Ishimaru, T. Yoshikawa, T. Masuda, C. Sakamoto, N. Kamimura, E. Masai, D. Takeuchi, T. Sonoki, Successful selective production of vanillic acid from depolymerized sulfite lignin and its application to poly(ethylene vanillate)

synthesis, Biores. Technol. 385 (2023) 129450, https://doi.org/10.1016/j.biortech.2023.129450.
[4] L. Mialon, R. Vanderhenst, A.G. Pemba, S.A. Miller, Polyalkylenehydroxybenzoates (PAHBs): biorenewable aromatic/aliphatic polyesters from lignin, Macromol. Rapid Commun. 32 (2011) 1386–1392, https://doi.org/10.1002/marc.201100242.
[5] C. Gioia, M.B. Banella, P. Marchese, M. Vannini, M. Colonna, A. Celli, Advances in the synthesis of bio-based aromatic polyesters: novel copolymers derived from vanillic acid and caprolactone, Polym. Chem. 7 (2016) 5396–5406, https://doi.org/10.1039/C6PY00908E.
[6] C. Fodor, M. Golkaram, A.J. Woortman, J. van Dijken, K. Loos, Enzymatic approach for the synthesis of biobased aromatic–aliphatic oligo-/polyesters, Polym. Chem. 8 (44), 6795–6805, https://doi.org/10.1039/C7PY01559C..
[7] C. Gioia, M.B. Banella, G. Totaro, M. Vannini, P. Marchese, M. Colonna, L. Sisti, A. Celli, Biobased vanillic acid and ricinoleic acid: building blocks for fully renewable copolyesters, J. Renew. Mater. 6 (2018) 126–135, https://doi.org/10.7569/JRM.2017.634191.
[8] A. Zamboulis, L. Papadopoulos, Z. Terzopoulou, D.N. Bikiaris, D. Patsiaoura, K. Chrissafis, M. Gazzano, N. Lotti, G.Z. Papageorgiou, Synthesis, thermal properties and decomposition mechanism of poly (ethylene vanillate) polyester, Polymers 11 (2019) 1672, https://doi.org/10.3390/polym11101672.
[9] M. Vannini, G. Giacobazzi, P. Marchese, C. Gioia, C. Marega, M.C. Righetti, A. Celli, From biomass to bio-based polymers: exploitation of vanillic acid for the design of new copolymers with tunable properties, Macromol. Chem. Phys. 224 (2023) 2300001, https://doi.org/10.1002/macp.202300001.
[10] E. Xanthopoulou, P.A. Klonos, A. Zamboulis, Z. Terzopoulou, A. Kyritsis, P. Pissis, D.N. Bikiaris, G.Z. Papageorgiou, Molecular mobility investigation of the biobased Poly(ethylene vanillate) and Poly(propylene vanillate), Polymer 233 (2021) 124197, https://doi.org/10.1016/j.polymer.2021.124197.
[11] A.A. Minakov, D.A. Mordvintsev, C. Schick, Melting and reorganization of poly (ethylene terephthalate) on fast heating (1000K/s), Polymer 45 (2004) 3755–3763, https://doi.org/10.1016/j.polymer.2004.03.072.
[12] P. Pan, Y. Inoue, Polymorphism and isomorphism in biodegradable polyesters, Prog. Polym. Sci. 34 (2009) 605–640, https://doi.org/10.1016/j.progpolymsci.2009.01.003.
[13] M.C. Righetti, P. Marchese, M. Vannini, A. Celli, C. Lorenzetti, D. Cavallo, C. Ocando, A.J. Müller, R. Androsch, Polymorphism and multiple melting behavior of bio-based poly(propylene 2,5-furandicarboxylate), Biomacromolecules 21 (2020) 2622–2634, https://doi.org/10.1021/acs.biomac.0c00039.
[14] H. Marand, A. Alizadeh, R. Farmer, R. Desai, V. Velikov, Influence of structural and topological constraints on the crystallization and melting behavior of polymers. 2. Poly(arylene ether ether ketone), Macromolecules 33 (2000) 3392–3403, https://doi.org/10.1021/ma9913562.
[15] Y. Furushima, M. Nakada, K. Ishikiriyama, A. Toda, R. Androsch, E. Zhuravlev, C. Schick, Two crystal populations with different melting/reorganization kinetics of isothermally crystallized polyamide 6, J. Polym. Sci., Polym. Phys. 54 (2016) 2126–2138, https://doi.org/10.1002/polb.24123.
[16] M.C. Righetti, M.L. Di Lorenzo, D. Cavallo, A.J. Müller, M. Gazzano, Structural evolution of poly(butylene succinate) crystals on heating with the formation of a dual lamellar population, as monitored by temperature-dependent WAXS/SAXS analysis, Polymer 268 (2023) 125711, https://doi.org/10.1016/j.polymer.2023.125711.
[17] A. Wurm, M. Merzlyakov, C. Schick, Reversible melting probed by temperature modulated dynamic mechanical and calorimetric measurements, Colloid Polym. Sci. 276 (1998) 289–296, https://doi.org/10.1007/s003960050242.
[18] R. Androsch, I. Moon, S. Kreitmeier, B. Wunderlich, Determination of heat capacity with a Sawtooth−Type, power compensated temperature modulated DSC, Thermochim. Acta 357–358 (2000) 267–278, https://doi.org/10.1016/S0040-6031(00)00397-X.
[19] M.C. Righetti, D. Prevosto, E. Tombari, Time and temperature evolution of the rigid amorphous fraction and differently constrained amorphous fractions in PLLA, Macromol. Chem. Phys. 217 (2016) 2013–2026, https://doi.org/10.1002/macp.201600210.
[20] A.M. Hindele, D.J. Johnson, The resolution of multipeak data in fibre science, J. Phys. D Appl. Phys. 4 (1971) 259–263, https://doi.org/10.1088/0022-3727/4/2/311.
[21] B.S. Hsiao, K.C.H. Gardner, D.Q. Wu, B. Chu, Time-resolved X-ray study of poly (aryl ether ether ketone) crystallization and melting behavior: 1. Crystallization, Polymer 34 (1993) 3986–3995, https://doi.org/10.1016/0032-3861(93)90658-W.
[22] B. Goderis, H. Reynaers, M.H.J. Koch, V.B.F. Mathot, Use of SAXS and linear correlation functions for the determination of the crystallinity and morphology of semic-crystalline polymers. Application to linear polyethylene, J. Polym. Sci. Polym. Phys. 37 (1999) 1715–1738, https://doi.org/10.1002/(SICI)1099-0488(19990715)37:14<1715::AID-POLB15>3.0.CO;2-F.
[23] Y. Kong, J.N. Hay, Multiple melting behaviour of poly(ethylene terephthalate), Polymer 44 (2003) 623–633, https://doi.org/10.1016/S0032-3861(02)00814-5.
[24] H. Xu, B.S. Ince, P. Cebe, Development of the crystallinity and rigid amorphous fraction in cold-crystallized isotacticpolystyrene, J. Polym. Sci. Polym. Phys. 41 (2003) 3026–3036, https://doi.org/10.1002/polb.10625.
[25] M.C. Righetti, M.L. Di Lorenzo, E. Tombari, M. Angiuli, The low-temperature endotherm in poly(ethylene terephthalate): partial melting and rigid amorphous fraction mobilization, J. Phys. Chem. B 112 (2008) 4233–4241, https://doi.org/10.1021/jp076399w.
[26] A.A. Minakov, A. Wurm, C. Schick, Superheating in linear polymers studied by ultrafast nanocalorimetry, Eur. Phys. J. E 23 (2007) 43–53, https://doi.org/10.1140/epje/i2007-10173-8.
[27] R. Zhang, K. Jariyavidyanont, E. Zhuravlev, C. Schick, R. Androsch, Zero-entropy-production melting temperature of crystals of poly(butylene succinate) formed at high supercooling of the melt, Macromolecules 55 (2022) 965–970, https://doi.org/10.1021/acs.macromol.1c02394.
[28] M.C. Righetti, M. Laus, M.L. Di Lorenzo, Rigid amorphous fraction and melting behavior of poly(ethylene terephthalate), Colloid Polym. Sci. 292 (2014) 1365–1374, https://doi.org/10.1007/s00396-014-3198-8.
[29] S. Rastogi, A.B. Spoelstra, J.G.P. Goossens, P.J. Lemstra, Chain mobility in polymer systems: on the borderline between solid and melt. 1. Lamellar doubling during annealing of polyethylene, Macromolecules 30 (1997) 7880–7889, https://doi.org/10.1021/ma970519o.
[30] H. Matsuda, T. Aoike, H. Uehara, T. Yamanobe, T. Komoto, Overlapping of different rearrangement mechanisms upon annealing for solution-crystallized polyethylene, Polymer 42 (2001) 5013–5021, https://doi.org/10.1016/S0032-3861(00)00893-4.
[31] T. Sawayanagi, T. Tanaka, T. Iwata, H. Abe, Y. Doi, K. Ito, T. Fujisawa, M. Fujita, Real-time synchrotron SAXS and WAXD studies on annealing behavior of poly[(R)-3-hydroxybutyrate] single crystals, Macromolecules 39 (2006) 2201–2208, https://doi.org/10.1021/ma052425h.
[32] C. Marega, V. Causin, A. Marigo, The morphology, structure and melting behaviour of cold crystallized isotactic polystyrene, Macromol. Res. 14 (2006) 588–595, https://doi.org/10.1007/BF03218729.
[33] H. Zhu, Y. Lv, T. Duan, M. Zhu, Y. Li, W. Miao, Z. Wang, In-situ investigation of multiple endothermic peaks in isomorphous poly(3-hydroxybutyrate-co-3-hydroxyvalerate) with low HV content by synchrotron radiation, Polymer 169 (2019) 1–10, https://doi.org/10.1016/j.polymer.2019.01.077.
[34] K.-N. Krüger, H.G. Zachman, Investigation of the melting behavior of poly(aryl ether ketones) by simultaneous measurements of SAXS and WAXS employing synchrotron radiation, Macromolecules 26 (1993) 5202–5208, https://doi.org/10.1021/ma00071a035.
[35] R. Verma, H. Marand, B. Hsiao, Morphological changes during secondary crystallization and subsequent melting in poly(ether ether keton) as studied by real time small angle X-ray scattering, Macromolecules 29 (1996) 7767–7775, https://doi.org/10.1021/ma951727o.
[36] A.M. Jonas, T.P. Russel, D.Y. Yoon, Synchrotron X-ray scattering studies of crystallization of poly(ether-ether-ketone) from the glass and structural changes during subsequent heating-cooling processes, Macromolecules 28 (1995) 8491–8503, https://doi.org/10.1021/ma00129a005.
[37] G.R. Strobl, M. Schneider, Direct evaluation of the electron density correlation function of partially crystalline polymers, J. Polym. Sci. Polym. Phys. 18 (1980) 1343–1359, https://doi.org/10.1002/pol.1980.180180614.
[38] B.S. Hsiao, R.K. Verma, A novel approach to extract morphological variables in crystalline polymers from time-resolved synchrotron SAXS data, J. Synchrotron Radiat. 5 (1998) 23–29, https://doi.org/10.1107/S0909049597010091.
[39] M.C. Righetti, E. Tombari, Crystalline, mobile amorphous and rigid amorphous fractions in poly(l-lactic acid) by TMDSC, Thermochim. Acta 522 (2011) 118–127, https://doi.org/10.1016/j.tca.2010.12.024.
[40] M.C. Righetti, M. Laus, M.L. Di Lorenzo, Temperature dependence of the rigid amorphous fraction in poly(ethylene terephthalate), Eur. Polym. J. 58 (2014) 60–68, https://doi.org/10.1016/j.eurpolymj.2014.06.005.
[41] M.C. Righetti, E. Tombari, M.L. Di Lorenzo, The role of the crystallization temperature on the nanophase structure evolution of poly[(R)-3-hydroxybutyrate], J. Phys. Chem. B 117 (2013) 12303–12311, https://doi.org/10.1021/jp4063127.
[42] M.C. Righetti, M.L. Di Lorenzo, Rigid amorphous fraction and multiple melting behavior in poly(butylene terephthalate) and isotactic polystyrene, J. Therm. Anal. Calorim. 126 (2016) 521–530, https://doi.org/10.1007/s10973-016-5553-0.